

Basal Plane Activation via Grain Boundaries in Monolayer MoS₂ for Carbon Dioxide Reduction

Ying Zhao, Yiqing Chen, Pengfei Ou,* and Jun Song*



Cite This: ACS Catal. 2023, 13, 12941–12951



Read Online

ACCESS |

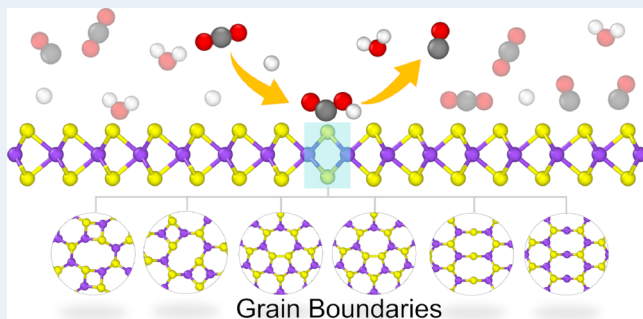
Metrics & More

Article Recommendations

Supporting Information

ABSTRACT: With the electrochemical carbon dioxide reduction reaction (CO₂RR) being a promising method to reduce atmospheric carbon dioxide (CO₂), transition metal dichalcogenides (TMDCs), such as molybdenum disulfide (MoS₂), have recently risen as potential catalysts for CO₂RR. However, pristine TMDCs are bottlenecked by the insufficiency of active sites in the basal plane. In this study, focusing on polycrystalline MoS₂, we perform systematic density functional theory calculations to investigate the role of grain boundaries (GBs) on the catalytic performance of MoS₂ for CO₂RR. Our results show that most GBs contribute to lowering the reaction energy of the potential-limiting step in CO₂RR. This effect can be further amplified with the introduction of S vacancies. In addition, the introduction of GBs with vacancies is shown to act as an effective method to break the scaling relations between reaction intermediates, which is crucial in improving catalytic efficiencies. Our findings demonstrate that defect engineering holds great potential to activate the basal plane of TMDCs for CO₂RR, providing valuable insights into engineering TMDCs for high-performing CO₂RR electrocatalysts.

KEYWORDS: *electrocatalysis, carbon dioxide reduction reaction, transition-metal dichalcogenides, grain boundaries, defect engineering, density functional theory*



1. INTRODUCTION

Carbon dioxide (CO₂) is the primary greenhouse gas emitted into the atmosphere through human activities. Its increasing atmospheric concentration over the years has been regarded as one dominant factor causing global climate change and thus a significant concern worldwide.^{1,2} To mitigate the adverse effects of CO₂ emissions, there have been notable efforts in recent years on CO₂ reduction.^{3–6} Among those efforts, the electrochemical CO₂ reduction reaction (CO₂RR) has been perceived as an appealing route since it can produce easily tunable products under ambient conditions.^{6–11}

The efficiency of electrochemical CO₂RR critically depends on catalyzing the electrochemical conversion of CO₂ to the desired fuels and chemicals. Currently, the electrocatalysts for CO₂RR processes are predominantly metals, particularly noble metals such as gold (Au),^{12–14} copper (Cu),^{15–18} silver (Ag),^{19,20} and palladium (Pd)^{21–23} due to their high conductivities, which facilitate charge transfer and high selectivity toward desired products, and therefore are regarded as better electrocatalysts for CO₂RR.^{24,25} However, these materials suffer from high costs and low accessibility, thus, impeding their large-scale applications. Consequently, researchers are motivated to search for alternative catalytic materials. In this search, two-dimensional (2D) materials, such as graphene, transition-metal dichalcogenides (TMDCs), and

black phosphorus, have attracted enormous interest due to their unique electrical and physical properties.¹¹ Among the 2D material group, TMDCs emerge with great potential thanks to their low-cost,^{26,27} mechanical flexibility,²⁸ relatively high carrier mobility,^{29,30} and tunable electronic structures,^{31–34} factors leading to favorable catalytic performance, while without suffering shortcomings, e.g., low stiffness,³⁵ low conductivity,^{36,37} and low degrees of freedom for structural transformation³⁸ in other popular 2D materials. As such, numerous studies have been conducted to investigate 2D TMDCs as potential catalysts for a wide range of chemical reactions involving CO₂RR.^{39–43} For instance, Asadi et al. reported that nanoflake tungsten diselenide (WSe₂) edges and layer-stacked molybdenum disulfide (MoS₂) with Mo-terminated edges could offer higher current densities and lower overpotentials to outperform common metal catalysts in CO₂RR.^{44,45} Abbasi et al. discovered that the required overpotential for CO₂RR at the edges of MoS₂ could be

Received: July 9, 2023

Revised: August 25, 2023

Published: September 20, 2023



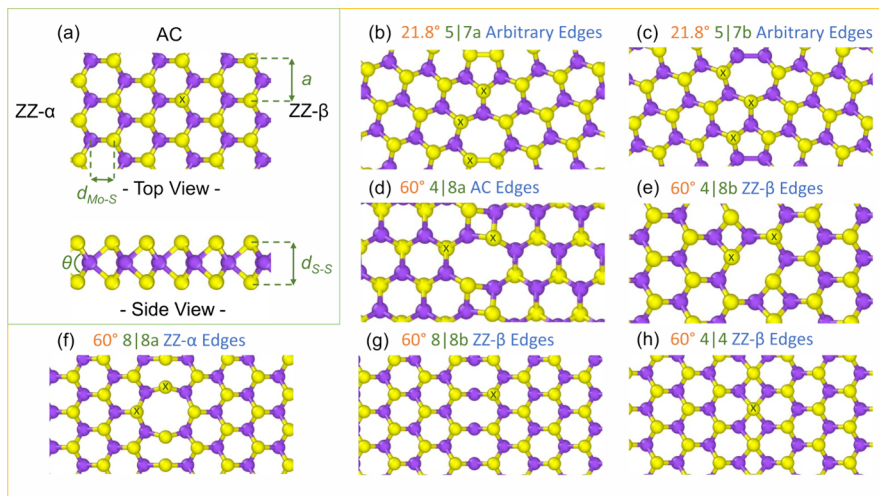


Figure 1. (a) Top and side views of pristine 2H MoS₂ with AC and ZZ edges, where a , $d_{\text{Mo-S}}$, $d_{\text{S-S}}$, and θ denote the lattice constant, the Mo–S bond length, the distance between the upper and lower sulfur atoms, and the S–Mo–S bond angle, respectively. Top views of (b) 5|7a, (c) 5|7b, (d) 4|8a, (e) 4|8b, (f) 8|8a, (g) 8|8b, and (h) 4|4 GBs. In these figures, Mo and S atoms are shown as purple and yellow spheres, respectively. Possible S vacancy sites are marked by 'X'. Tilting angles, ring compositions, and edge types are labeled from left to right on top of each GB structure.

further lowered by doping.⁴⁶ Li et al. found that the edge-exposed 2H MoS₂ hybridized with N-doped carbon could enrich active sites and reduce the energy required for the potential-limiting step for CO₂RR.⁴⁷ In contrast to the ability of TMDC edges to catalyze CO₂RR, the basal plane of a TMDC is generally catalytically inert.^{48–50} With the edge sites constituting only a small fraction of the available sites, this becomes a critical bottleneck to the practical application of 2D TMDCs as CO₂RR electrocatalysts and necessarily calls for means to activate the TMDC basal plane.

Despite the perceived basal inertness of TMDCs in the CO₂RR, one aspect that remains elusive is the role of lattice defects in affecting the catalytic properties of TMDCs. Lattice defects are unavoidably introduced during conventional fabrication of TMDCs.^{51,52} In various other material systems (e.g., Cu and Au), it has been shown that the catalytic activities of materials may be enhanced by introducing and/or manipulating the lattice defects, namely defect engineering.⁵³ The effectiveness of defect engineering in other material systems has motivated many studies of lattice defects in TMDCs, both experimentally^{54–57} and theoretically.^{54,58,59} Among the various lattice defects, grain boundaries (GBs) are one category that is prevailing, particularly in large-scale fabrications of TMDCs. For instance, chemical vapor deposition (CVD) of TMDCs results in domains of different crystalline orientations and thus abundant GBs.⁶⁰ It has been demonstrated that sites at GBs tend to be more active and can facilitate catalytic reactions, such as the hydrogen evolution reaction (HER),^{61–65} CO₂RR,^{66–68} oxygen reduction and evolution reaction (ORR and OER),^{69–73} and nitrogen reduction reaction (NRR)^{74,75} in various material systems. Meanwhile, GBs also serve as locations for segregation of other defects, such as vacancies, self-interstitials, and antisite defects.^{76–79} However, despite the potential of GBs in facilitating various catalytic reactions, the effects of GBs and their interplay with other defects on the CO₂RR catalytic activity of TMDCs remain elusive.

In the present study, we investigated the possibility of utilizing GBs toward basal plane activation of TMDCs for CO₂RR, employing systematic first-principles density func-

tional theory (DFT) calculations. MoS₂ was selected as the representative TMDC system due to its earth abundancy nature, which enables its large-scale production,^{80–82} and its 2H phase was assumed due to its thermodynamical stability compared to other phases.⁸³ Different GBs in MoS₂ were constructed with their formation energies examined, followed by the energy profiles of the CO₂RR at these GBs being calculated. Then, the interplay between vacancies and GBs was considered, and its effect on the CO₂RR at GBs was studied. In the end, by evaluating scaling relations between reaction intermediates and structural and electronic properties of different systems, we proposed ways to potentially activate the inert basal plane of TMDCs, which shed light on GB engineering toward CO₂RR.

2. COMPUTATIONAL METHODS

2.1. Structures and Formation Energies of GBs.

Starting with the periodic unit cell of 2H MoS₂, we first optimized the geometries to obtain the equilibrium lattice parameters. As indicated in Figure 1a, the lattice constant (a), the Mo–S bond length ($d_{\text{Mo-S}}$), the distance between the upper and lower sulfur atoms ($d_{\text{S-S}}$), and the S–Mo–S bond angle (θ) of pristine 2H MoS₂ were determined to be 3.19 Å, 2.41 Å, 3.12 Å, and 80.54°, respectively, all in good agreement with previous studies.^{84,85}

We then constructed and optimized a series of GBs of different tilt angles (i.e., ranging from 21.8° to 60°), with their atomic configurations illustrated in Figure 1b–h. The GBs were constructed using nanoribbon (NR) models with chiral edges containing zigzag (ZZ) and/or armchair (AC) structures (see Figure 1a). NR widths greater than 35 Å were ensured to avoid GB-edge interactions. We note that the NR model was also used for pristine MoS₂ for consistency in the energy calculations.

Depending on the tilt angle, the NR structures show different geometrical characteristics at the GBs and edges. For instance, for the 60°-tilt GBs, the NRs obtained may consist of ZZ- α , ZZ- β , or AC edges, depending on the type of GBs, as shown in Figure 1d–h. On the other end, for the 21.8°-tilt

GBs, the edges are arbitrary combinations of ZZ and AC sites, as shown in Figure 1b,c. The ring units constituting the GB vary greatly for different GBs, and below we describe GBs in terms of their ring compositions. For example, the 21.8°-tilt GBs are composed of pentagon-heptagon pairs periodically separated by one hexagonal ring (5|7a and 5|7b) (cf., Figure 1b,c), and the 60°-tilt GBs contain repeated (1) quadrangle–octagon pairs (4|8a and 4|8b), (2) octagon rings (8|8a and 8|8b), and (3) quadrangle rings (4|4) constituting the entire GB (c.f. Figure 1d–h). These GBs were constructed following the method described by Ouyang et al.,⁶⁵ and more details are provided in Figure 1.

Since GBs, edges, and chemical potential of Mo and S all contribute to the total energy of the MoS₂ NR model, the formation energy of a GB (or the GB energy) in MoS₂, denoted as $E_{\text{GB}}^{\text{MoS}_2}$, is calculated by

$$E_{\text{GB}}^{\text{MoS}_2} = \frac{E_{\text{tot}} - \mu_S \times N_S - \mu_{\text{Mo}} \times N_{\text{Mo}}}{L} - E_{\text{Edge},1} - E_{\text{Edge},2} \quad (1)$$

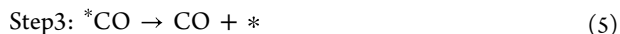
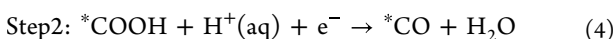
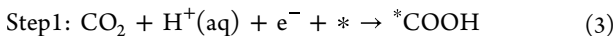
where E_{tot} is the energy of the entire NR structure with GB; $E_{\text{Edge},1}$ and $E_{\text{Edge},2}$ are the energy of each edge per unit length; L is the length of the NR; μ_S and μ_{Mo} are the chemical potentials of S and Mo, respectively; N_S and N_{Mo} are the numbers of S and Mo atoms in the GB structure, respectively. More details on $E_{\text{GB}}^{\text{MoS}_2}$ calculations are provided in Section I of the Supporting Information.

2.2. Vacancy Defects and Vacancy Formation Energies on MoS₂ GBs. Since S single vacancies (SVs) tend to form more easily on MoS₂ GBs under both Mo-rich and S-rich conditions compared to other defects such as Mo SVs,⁸⁶ here we introduced S SVs at different MoS₂ GBs. In addition, by introducing S SVs, the Mo atoms can potentially be exposed to and form direct bonds with the adsorbates, which has proven to be an effective method to increase the surface catalytic activities.^{87,88} Possible S vacancy sites are marked in Figure 1. The formation energy of an SV of substance i , E_v^i , is calculated by

$$E_v^i = E_v - E + \mu_i \quad (2)$$

where E and E_v are the energies of pristine and defective GB systems, respectively, and μ_i is the chemical potential of elemental S, taking the chemical potentials of 1/8 S₈ as a reference. The results are provided in Section II of the Supporting Information.

2.3. Gibbs Free Energy of the CO₂RR Process. The overall CO₂RR process proceeds at the electrode surface, in contact with the electrolyte.⁸⁹ Since carbon monoxide (CO) has a wide range of industrial applications,⁹⁰ and it can be produced into different organic chemical products,⁹¹ our study targets the CO₂ to CO conversion. As suggested by previous studies,^{90,92,93} a three-step reaction mechanism via a two-electron pathway is considered. During the first step (eq 3), a concerted proton–electron transfer occurs, which forms COOH adsorbed on the catalyst surface sites. The COOH is then reduced to adsorbed CO by accepting one proton–electron pair (eq 4). The adsorbed CO can be easily desorbed if the binding is weak enough (eq 5).



where the asterisk (*) indicates the surface adsorption site and * followed by a molecule denotes an adsorbed species. More information on adsorption sites is provided in Section IV of the Supporting Information. The first two steps are potential-dependent, while the last step is a desorption process that proceeds without proton/electron transfer.

The Gibbs free energy changes, ΔG of each reaction step (eqs 3–5) are calculated using the computational hydrogen electrode (CHE) model,⁹⁴ which can effectively model electrochemistry using data from first-principle calculations. The ΔG is calculated by subtracting the sum of Gibbs free energies, G , of the individual reactants from the products. For example, for step 1 (eq 3), $\Delta G = G_{*\text{COOH}} - (G_{1/2\text{H}_2} + G_{\text{CO}_2} + G_*)$, where the subscripts denote the species types. G is calculated by

$$G = E + E_{\text{corr}} \quad (6)$$

where E is the electronic energy of individual components and E_{corr} is the correction energy composed of zero-point energy (ZPE), entropy (S), and heat capacity (C_p), expressed by

$$E_{\text{corr}} = \text{ZPE} + \int C_p dT - TS \quad (7)$$

where T is the temperature taken as the room temperature (298.15 K). For more details, see Section V of the Supporting Information. With ΔG known, the theoretical limiting potential (U_L), under the applied potential of 0.0 V, can be obtained as

$$U_L = -\Delta G/e \quad (8)$$

where e is the charge on an electron.

2.4. Computational Details. All calculations were performed by employing spin-polarized DFT within a generalized gradient approximation parametrized by Perdew, Burke, and Ernzerhof (GGA-PBE), as implemented in the Vienna ab initio simulation package (VASP).^{95–99} The electron–ion potential was described by the projected-augmented wave (PAW) method,^{98,100} and a kinetic energy cutoff of 520 eV was used for the plane wave expansion. The Brillouin zone was sampled using a $1 \times 4 \times 1$ gamma-centered grid of k-points. All structures were relaxed until the atomic forces were less than 0.01 eV/Å and the total energies converged to 10^{-5} eV. The in-plane separation between the NR edges across periodic boundaries is set to be greater than 20 Å to avoid any artificial effect arising from edge–edge interactions. The vacuum spaces in all supercells were >15 Å above the MoS₂ plane to avoid any artificial interactions. The DFT-D2 method of Grimme was used to address any van der Waals (vdW) interactions resulting from dynamical correlations between fluctuating polarizations of molecules.¹⁰¹

3. RESULTS AND DISCUSSION

3.1. Formation Energies of MoS₂ Grain Boundaries. The formation energies for different MoS₂ GBs as functions of μ_S are presented in Figure 2. Generally, the formation energy lies between −0.75 and 2.17 eV/Å. We observe that under an S-rich environment, 8|8a, 5|7b, 5|7a, and 4|8a GBs are more likely to form, as indicated by their relatively low formation energies. Notably, 8|8a and 5|7b GBs exhibit negative $E_{\text{GB}}^{\text{MoS}_2}$ under S excess conditions, implying the possibility of their spontaneous formation under S-rich conditions. In contrast,

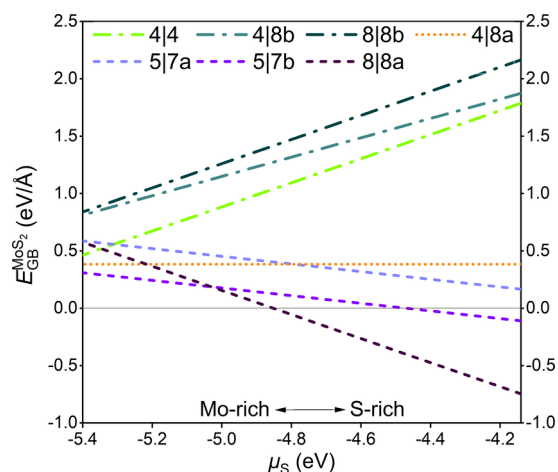


Figure 2. Formation energies ($E_{\text{GB}}^{\text{MoS}_2}$) of MoS_2 GBs as functions of chemical potential of elemental S (μ_S). Dash-dotted lines indicate a preferential formation under Mo-rich conditions, while dashed lines represent a favorable formation under S-rich conditions. The dotted line (4|8a GB) shows no preference of the chemical environment.

the preferences in GB types are more ambiguous under the Mo-rich condition as $E_{\text{GB}}^{\text{MoS}_2}$ values show a limited difference. For instance, the difference among all $E_{\text{GB}}^{\text{MoS}_2}$ values is less than 0.53 eV/Å at the Mo extremum.

3.2. Reaction Coordinates and Energetics of CO_2 RR at GBs. The free energy pathways of reduction of CO_2 to CO on MoS_2 GBs are presented in Figure 3a, with numeric details summarized in Section V of the Supporting Information. Among all elementary reaction steps, the activation of CO_2 triggering *COOH formation (i.e., reaction step 1) is the most endergonic step. The weak interaction between *CO and substrates (i.e., CO physisorption) results in the downward

behavior observed in the *CO desorption step (i.e., reaction step 3). The limiting potentials of all GB systems, except for 4|4 (2.28 eV), are lower than those of the pristine basal plane (2.20 eV). This lower potential indicates that grain boundaries can indeed break the inertia of the basal plane and enhance the interaction between *COOH and the adsorption site. This also seems to be a generic feature for many other TMDCs from our preliminary analysis (e.g., see preliminary results in Section III of the Supporting Information on the energetics of 2H WSe₂ GBs, where a similar trend was observed).

Although GBs show potential in enhancing catalytic CO_2 RR performance by lowering the reaction energy of MoS_2 basal plane, the energies at the potential-limiting step are still high (>1.00 eV, except for 8|8a which shows 0.65 eV), which may hinder reactions according to the Sabatier principle.¹⁰² This can lead to a preference for competing reactions, such as HER, which is unavoidable under aqueous conditions. More on HER and CO_2 RR competitions will be discussed in the Section 3.3.

Besides the GB itself, its role as a sink for point defects like S SVs (confirmed by the low formation energies of S SVs at GBs, see Section II of the Supporting Information) also comes into play in affecting the CO_2 RR. Thus, the CO_2 RR at S SVs decorated GBs were investigated, with the reaction energies presented in Figure 3b. All GBs, except for the case of 8|8a, show lower reaction energies for the potential-limiting step in the presence of the S SV. The *COOH formation step is observed to be the potential-limiting step for all cases except for the case of 4|4 SV GB, where *CO desorption dominates the reaction. These overall better catalytic activities in SV-decorated GBs can be rationalized by the change of binding sites after the addition of SVs (i.e., the 3p S bonding has changed to 4d Mo bonding). Figure 3 shows how the intermediate adsorbed atoms bond differently on 4|4 GB with and without SV. Notably, the reaction on 4|4 SV GB obtains the lowest reaction energy (0.31 eV), while it is thermody-

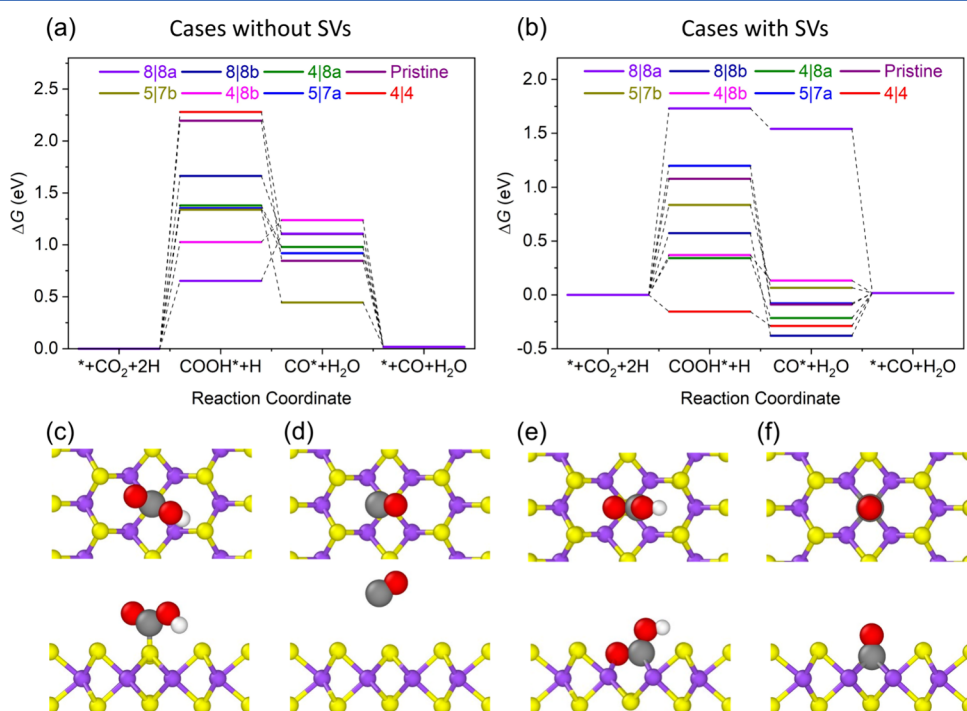


Figure 3. Energetics of the CO_2 RR process on MoS_2 GBs (a) without and (b) with the presence of S SVs. Top and side views of *COOH (c and e) and *CO (d and f) adsorptions on the MoS_2 4|4 GB as a representative, without (c and d) and with (e and f) the presence of S vacancies.

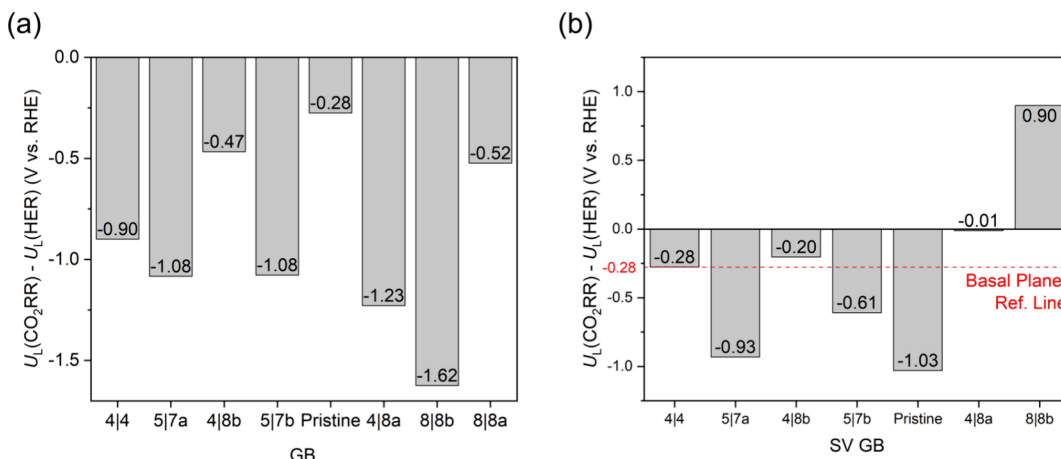


Figure 4. Difference between the CO₂RR and HER thermodynamic limiting potentials ($U_L(\text{CO}_2\text{RR}) - U_L(\text{HER})$) on different (a) pristine and (b) SV-decorated MoS₂ GBs, respectively. The red dotted line indicates the value for a pristine basal plane.

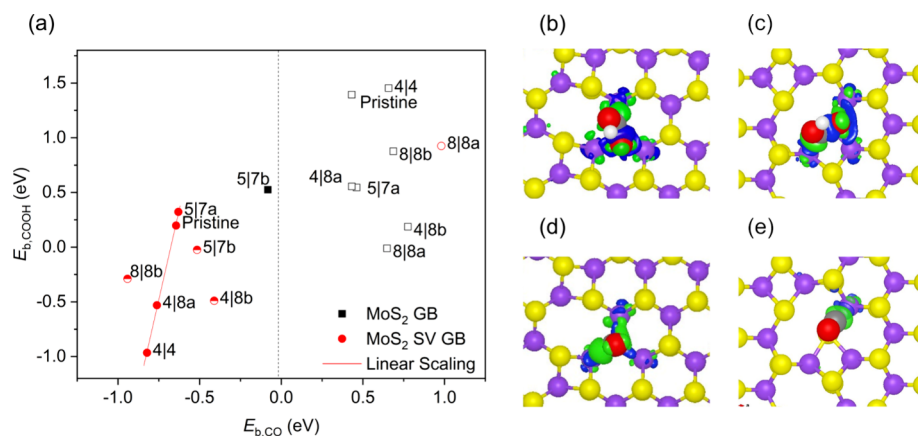


Figure 5. (a) Calculated binding energy between *COOH and *CO for the studied GB systems. The scaling relation among 4|4, 4|8a, and 5|7a SV GBs, as well as SV MoS₂ is shown using the red line. The half-shaded red dots represent SV GBs that do not obey the linear scaling. The vertical dotted line is the CO adsorption threshold. When $E_{b,\text{CO}}$ is greater than the threshold, CO gas is more likely to form, while when the binding energy is smaller than the threshold, CO is more likely to be further protonated into other products such as CH₄ (see Section VIII of the Supporting Information for details). Note that these CO binding energies include a 0.51 eV correction to account for the PBE error. (b, d) Adsorption isosurfaces of *COOH and *CO on 4|8a SV GBs, respectively, and (c, e) adsorption isosurfaces of *COOH and *CO on 4|8b SV GBs, respectively. The green and blue regions represent the charge density difference of +0.005 and -0.005 e Bohr⁻¹, respectively.

nically least favorable on the GB without adding an SV. Adsorption configurations for SV GB structures other than 4|4 are provided in Figure S4 of the Supporting Information.

It is also worth noting that the energies required for CO₂RR potential-limiting step on 8|8a GB, and 5|7b, 8|8b, 4|8b, 4|8a, and 4|4 SV GBs are lower than those on MoS₂ edges (around 0.9 eV according to Xie et al.¹⁰³), indicating a higher likelihood of the reaction occurring on the aforementioned GBs rather than the edges.

3.3. HER vs CO₂RR Selectivity. As shown above, the reaction energies of the CO₂RR can be reduced by GBs, and furthermore, more significantly decreased in the presence of SVs at GBs. However, besides the reaction energy, another important aspect necessitating consideration in assessing the CO₂RR performance is the suppression of the competing HER, an aspect essential to ensure high CO selectivity. Therefore, we calculated the reaction energies associated with H₂ evolutions on the SV-decorated GB structures. The HER energetics on pristine GBs are provided in the work published by Ouyang et al.⁶⁵ Since the difference between the thermodynamic limiting potentials for CO₂RR and HER

($U_L(\text{CO}_2\text{RR}) - U_L(\text{HER})$) is a good indicator of CO₂RR selectivity,^{104–106} we plot out the $U_L(\text{CO}_2\text{RR}) - U_L(\text{HER})$ in Figure 4. As seen from Figure 4a, when there is no SV added to the GBs, all GBs show more negative values compared with the pristine basal plane, indicating that all GB systems are prone to HER competition. On the other hand, for MoS₂ GBs decorated with SVs (Figure 4b), more positive values are observed for all GB systems compared to SV MoS₂, which indicates that all SV GBs obtained higher selectivity for CO₂ reduction to CO compared with SV incorporated basal plane. Notably, 4|4, 4|8b, 4|8a, and 8|8b SV GBs show better selectivity compared to the pristine basal plane (red dotted line in Figure 4b), indicative of their potential to selectively activate the inert MoS₂ basal plane for the CO₂RR. Note that 8|8a SV GB is excluded from this discussion due to its high energy at the potential-limiting step.

3.4. Break the Scaling Relation. Numerous efforts have been made to break the scaling relation between the intermediates in CO₂RR since the scaling relation prevents the adsorption energy of intermediates from being tuned independently and limits the catalytic efficiency of transition-

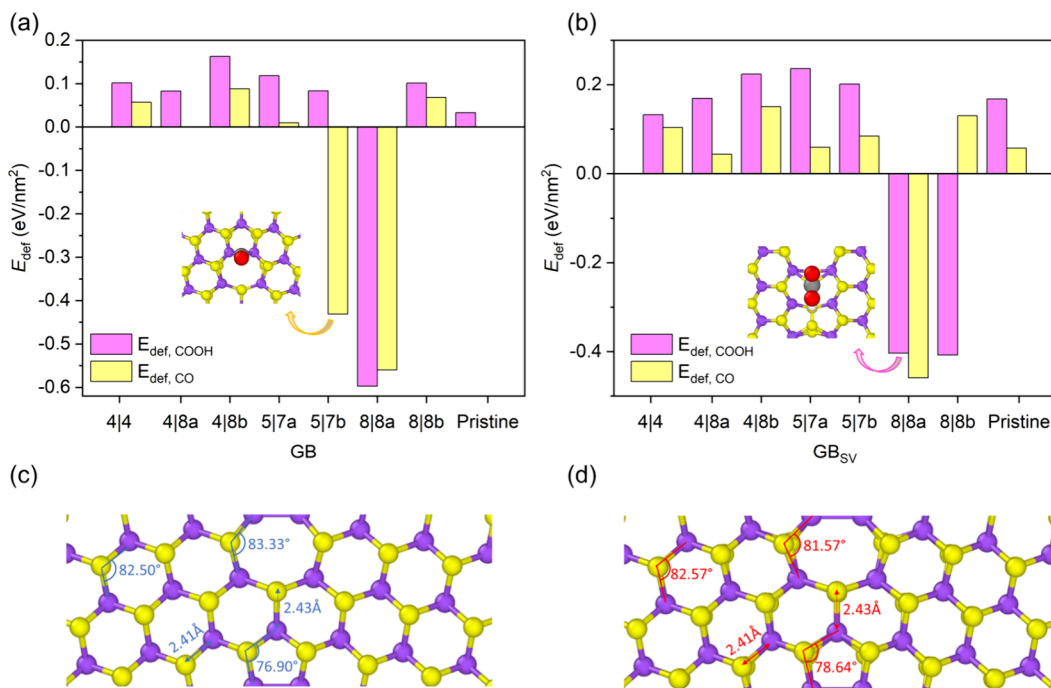


Figure 6. Substrate deformation energies for different (a) GBs and (b) SV GBs after $^{*}\text{CO}$ and $^{*}\text{COOH}$ adsorptions. Configurations of $^{*}\text{CO}$ adsorption on 5|7b GB and $^{*}\text{COOH}$ adsorption on 8|8a SV GB are displayed in parts (a) and (b), respectively. (c) and (d) show the local deformation of the 5|7b GB before and after CO adsorptions, respectively.

metal catalysts.¹⁰⁷ Reducing coordination numbers,^{108,109} doping p-elements,¹¹⁰ introducing oxophilic adsorption sites,¹¹¹ separating intermediates on different active sites,^{67,112} tethering active ligands,¹¹³ and strain engineering¹¹⁴ are all possible methods to break such scaling relations.

The scaling relation for the binding energies between $^{*}\text{COOH}$ and $^{*}\text{CO}$ on MoS_2 GB and SV GBs is shown in Figure 5a. Since $^{*}\text{CO}$ is physisorbed to the pristine GBs except for 5|7b, no apparent scaling relation is observed. For specific chemisorbed species, a linear scaling relation becomes evident, notably within the 4|4, 4|8a, and 5|7a SV GBs, along with the pristine basal plane with SV, as indicated by the red line in Figure 5a. More detail on the linear scaling relation is provided in Section IX of the Supporting Information. However, other chemisorbed species, namely 8|8b, 5|7b, and 4|8b SV GBs, show deviations from the linear relation. For structures conforming to the linear line, we observed that the intermediate species, namely $^{*}\text{COOH}$ and $^{*}\text{CO}$, attained the same bonding coordination as well as consistent adsorption sites. This stands in clear contrast to structures that deviate from the linear line, where dissimilar adsorption configurations are observed for the intermediate species. For example, on 4|8b SV GB, COOH bonds with three Mo atoms while CO bonds with one, which decouples the binding energies, while on 4|8a SV GB, both $^{*}\text{COOH}$ and $^{*}\text{CO}$ bond with 3 Mo on the same site (Figure 5b–e). Moreover, when introducing SVs on pristine GBs, we can effectively reduce the coordination numbers of GB sites and introduce sites that can additionally bond with O in the adsorbates, which explains why the binding energies of intermediates on pristine 5|7b GB depart from the scaling relation.

3.5. Substrate Deformations. During the adsorption step, we observed some reconstruction in the substrate, indicative of deformation induced by the adsorption. Such deformation may have a profound impact on site selectivity

and catalytic activity.^{116,117} Specifically, adsorption can induce deformation strains on the host surface, resulting in the generation of surface stress and a subsequent decrease in surface energy. This reduction in surface energy can be advantageous by minimizing the overall energy of the adsorbate-modified system. Conversely, the migration of atoms may lead to blockage of the adsorption site and, consequently, deactivate the site. Therefore, it is important to quantify the degree of deformation, for which we calculated the substrate deformation energy (E_{def}) to estimate the degree of substrate deformation caused by the adsorption of a reaction intermediate:

$$E_{\text{def}} = \frac{E_{\text{sub,f}} - E_{\text{sub,i}}}{A} \quad (9)$$

where $E_{\text{sub,i}}$ and $E_{\text{sub,f}}$ are the energies of the substrate before and after adsorptions, respectively, and A is the area of the substrate. Note that although the deformation at GBs can be rather localized, the range of such localization varies from GB to GB (e.g., Figure 6c,d) and is hard to define. Consequently, we use E_{def} global deformation energy of the entire substrate structure (per unit area), instead. Despite E_{def} not capturing the deformation localization, it provides a rough measure of the overall degree of deformation.

Figure 6a, b provide the substrate deformation energies for different studied systems after $^{*}\text{CO}$ and $^{*}\text{COOH}$ adsorptions. On the one hand, structural deformation can mitigate the effect of bonding. For example, strong bonding is observed between C and Mo for CO adsorption at the MoS_2 5|7b GB, indicating endothermic $^{*}\text{CO}$ desorption. However, due to the large deformation of such a GB (Figure 6a), the effect of bonding is mitigated, resulting in a negative slope during $^{*}\text{CO}$ desorption (i.e., exothermic). On the other hand, the deformation-induced reconstruction may lead to a less desirable structure for adsorption. For example, the deformation rendered 8|8a SV

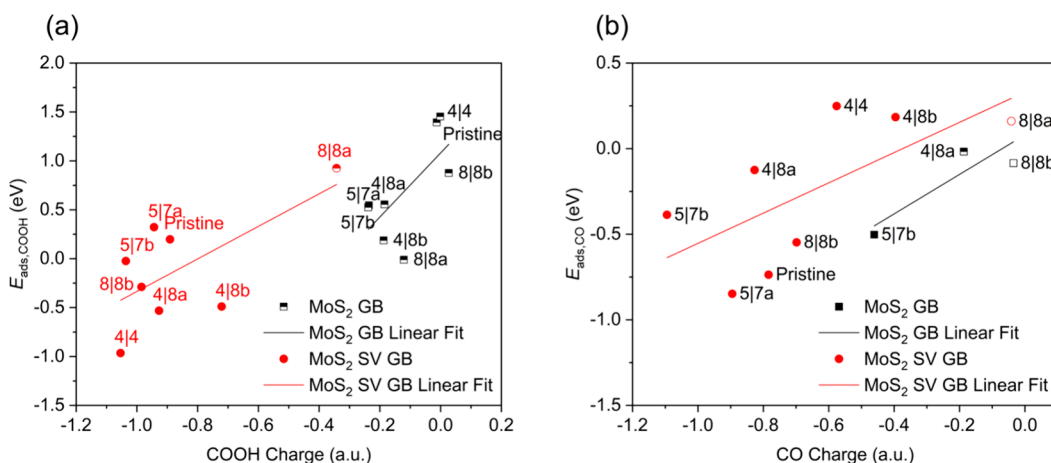


Figure 7. Number of excess charges on (a) COOH and (b) CO for the studied systems, with respect to adsorption energies, with their correlations marked by the straight lines. Fully shaded and half-shaded symbols are used for adsorbates bonded to Mo and S, respectively, and hollow symbols represent physisorbed species. Note that only one physisorbed *CO was chosen for plain and SV GBs, whose $E_{\text{ads,CO}}$ is the closest to average physisorbed *CO $E_{\text{ads,CO}}$, for a better demonstration.

GB to reconstruct into a more stable configuration without active Mo exposure after *COOH formation (Figure 6b), which substantially suppressed the catalytic activity. It is, however, important to note that structural characteristics are not the sole factors affecting catalytic activities. There are other factors, in particular the electronic properties, which play a critical role and will be discussed in the following section.

3.6. Electronic Properties. As many studies have demonstrated a strong link between catalytic activities and electronic properties,^{70,118,119} we further investigated the electronic properties to understand the rationale for the changes in adsorption behaviors. Energy analysis by Huang et al. revealed that the closer an electronic state is to the Fermi energy, E_F , the greater its contribution to bonding.¹²⁰ Therefore, density of states (DOS) calculations were performed for various cases. Figure S5a and b provide the DOS plots for adsorptions on MoS₂ pristine basal plane and 5|7b GB, respectively. *COOH adsorption on pristine MoS₂ surface shows sulfur 3p bonding state hybrid with carbon 2p state at around -11.0 eV. In comparison, the hybridization on 5|7b GB occurs at about -8.0 eV, which is closer to E_F , indicating stronger bonding at 5|7b GB. The DOS of *CO adsorption on 5|7b GB shows CO bonding with the Mo 4d state, whereas no bonding is observed for that on the pristine basal plane. It is notable that we also noticed conductivity changes with the introduction of defects. For example, with the introduction of 4|8b GB on MoS₂, E_F becomes filled with energy states, indicating its conductive behavior, which can potentially enhance the carrier mobility of pristine MoS₂ that is inherently a semiconductor, as shown in Figure S5c.

Charge transfer, another descriptor for CO₂RR,¹²¹ has been obtained using the Bader charge analysis.¹²² Figure 7 provides the number of charges transferred from the substrates to the adsorbates corresponding to adsorption energies. Most data points for CO physisorption are excluded in the figure due to the minuscule number of electrons transferred (i.e., weak vdW forces dominant). The numeric details are provided in Table S8 in the Supporting Information. Generally, lower adsorption energies are observed when more charges are transferred from the catalyst to the adsorbates. By creating SVs on GBs, we efficiently increase the charge transferred from the substrates to the adsorbates and therefore enhance the catalytic activity.

However, though a clear correlation between the adsorption energy and charge transfer can be observed (c.f. Figure 7), the relationship is not well-defined, as indicated by the deviation of data points from the linear fitting. This is possibly due to different degrees of lattice deformation during the reactions for different systems. In addition, ligancy, or coordination numbers, which describes the number of nearest neighbors that a surface site bonds to,¹²³ is another descriptor for CO₂RR that strongly correlates with charge transfers.¹²⁴ A higher coordination number corresponds to stronger bonding and more charge transferred. As shown in Table S9 in the Supporting Information, the binding energy decreases with an increasing coordination number of C, except for 8|8b, obtaining low ligancy but strong binding. This 8|8b peculiarity is probably due to the substantial structural deformation experienced by GB structure induced by the *CO adsorption.

4. CONCLUSIONS

In summary, the present study systematically examined GBs as a potential means to activate the basal plane of MoS₂ for enhanced CO₂RR performance by employing first-principles calculations. GBs can enhance the catalytic performance of MoS₂ by decreasing the energy required by the potential-limiting step. The interactions between *CO and the GBs are relatively weak, facilitating the desorption of *CO as gaseous CO. Introducing S vacancies to GBs serves to further reduce the limiting potential, owing to strong bonds formed between adsorbates and undercoordinated vacancy sites. The steady *CO adsorption is a critical precursor for subsequent reduction to various other hydrocarbon products. Our electronic analysis showed that augmented binding strength between substrate and adsorbate arises from escalated charge transfer, attainable through the exposure of undercoordinated substrate sites. Substrate deformation is another factor that strongly impacts the binding behavior. We also discovered that, by changing the binding sites of intermediates and reducing the coordination numbers at the adsorption sites, GBs make it possible to disrupt the conventional scaling relation. In terms of selectivity, 4|4, 4|8b, 4|8a, and 8|8b SV GBs show better performance toward CO₂RR over the competing HER compared to the pristine basal plane.

Our findings show that GBs and S vacancies synergistically offer a viable defect engineering route to activate the inert MoS₂ basal plane toward CO₂RR, providing valuable insights toward designing a new class of high-performance CO₂RR electrocatalysts.

■ ASSOCIATED CONTENT

§ Supporting Information

The Supporting Information is available free of charge at <https://pubs.acs.org/doi/10.1021/acscatal.3c03113>.

Calculations of GB formation energies; vacancy formation energy data; Gibbs free energy diagrams of WSe₂ GBs; schematic of intermediate adsorption sites; data of Gibbs free energy calculations; substrate deformation energies after adsorption; electronic characteristics of investigated systems; subsequent reduction of *CO; and scaling linear regression ([PDF](#))

■ AUTHOR INFORMATION

Corresponding Authors

Pengfei Ou – Department of Chemistry, Northwestern University, Evanston, Illinois 60208, United States;
Email: pengfei.ou@northwestern.edu

Jun Song – Department of Mining and Materials Engineering, McGill University, Montreal, Quebec H3A 0C5, Canada;
[ORCID: 0000-0003-3675-574X](https://orcid.org/0000-0003-3675-574X); Email: jun.song2@mcgill.ca

Authors

Ying Zhao – Department of Mining and Materials Engineering, McGill University, Montreal, Quebec H3A 0C5, Canada; [ORCID: 0000-0003-3865-9890](https://orcid.org/0000-0003-3865-9890)

Yiqing Chen – Department of Mining and Materials Engineering, McGill University, Montreal, Quebec H3A 0C5, Canada; [ORCID: 0000-0002-2686-5593](https://orcid.org/0000-0002-2686-5593)

Complete contact information is available at:

<https://pubs.acs.org/10.1021/acscatal.3c03113>

Author Contributions

Y.Z., P.O., and J.S. conceived the idea. Y.Z. carried out the DFT computations and data analysis and wrote the paper. P.O. and J.S. supervised the project and cowrote the paper. Y.C. participated in the discussion and polished the paper. All authors discussed the results and assisted during the manuscript preparation.

Notes

The authors declare no competing financial interest.

■ ACKNOWLEDGMENTS

This work was financially supported by the Natural Sciences and Engineering Research Council of Canada Discovery Grant (RGPIN-2017-05187) and the McGill Engineering Doctoral Award (MEDA). The computational resource was provided by the Digital Alliance of Canada.

■ REFERENCES

- (1) Schneider, S. H.; Rosencranz, A.; Mastrandrea, M. D.; Kuntz-Duriseti, K. *Climate Change Science and Policy*. Island Press: Washington, United States, 2009.
- (2) Tucker, L.; Sherwood, L. *Understanding Climate Change*; National Science Teachers Association: Arlington, VA, United States, 2019.
- (3) Mikkelsen, M.; Jørgensen, M.; Krebs, F. C. The teraton challenge. A review of fixation and transformation of carbon dioxide. *Energy Environ. Sci.* **2010**, *3* (1), 43–81.
- (4) Marken, F.; Fermin, D. *Electrochemical reduction of carbon dioxide: overcoming the limitations of photosynthesis*; Royal Society of Chemistry: Cambridge, 2018.
- (5) Reina, T. R.; Odriozola, J. A.; Arellano-Garcia, H. *Engineering solutions for CO₂ conversion*; Wiley-VCH: Weinheim, 2021.
- (6) Qiao, J.; Liu, Y.; Zhang, J. *Electrochemical reduction of carbon dioxide: fundamentals and technologies*. CRC Press: Boca Raton, 2016.
- (7) Lu, Q.; Jiao, F. Electrochemical CO₂ reduction: Electrocatalyst, reaction mechanism, and process engineering. *Nano Energy* **2016**, *29*, 439–456.
- (8) Xie, Y.; Li, X.; Wang, Y.; Li, B.; Yang, L.; Zhao, N.; Liu, M.; Wang, X.; Yu, Y.; Liu, J.-M. Reaction mechanisms for reduction of CO₂ to CO on monolayer MoS₂. *Appl. Surf. Sci.* **2020**, *499*, No. 143964, DOI: [10.1016/j.apsusc.2019.143964](https://doi.org/10.1016/j.apsusc.2019.143964).
- (9) Khezri, B.; Fisher, A. C.; Pumera, M. CO₂ reduction: the quest for electrocatalytic materials. *J. Mater. Chem. A* **2017**, *5*, 8230–8246.
- (10) Zhang, L.; Zhao, Z. J.; Gong, J. Nanostructured Materials for Heterogeneous Electrocatalytic CO₂ Reduction and their Related Reaction Mechanisms. *Angew. Chem., Int. Ed.* **2017**, *56* (38), 11326–11353.
- (11) Sun, Z.; Ma, T.; Tao, H.; Fan, Q.; Han, B. Fundamentals and Challenges of Electrochemical CO₂ Reduction Using Two-Dimensional Materials. *Chem.* **2017**, *3* (4), 560–587.
- (12) Zhu, W.; Michalsky, R.; Metin, O.; Lv, H.; Guo, S.; Wright, C. J.; Sun, X.; Peterson, A. A.; Sun, S. Monodisperse Au nanoparticles for selective electrocatalytic reduction of CO₂ to CO. *J. Am. Chem. Soc.* **2013**, *135* (45), 16833–16836.
- (13) Yang, D.-R.; Liu, L.; Zhang, Q.; Shi, Y.; Zhou, Y.; Liu, C.; Wang, F.-B.; Xia, X.-H. Importance of Au nanostructures in CO₂ electrochemical reduction reaction. *Sci. Bull.* **2020**, *65* (10), 796–802.
- (14) Fang, Y.; Cheng, X.; Flake, J. C.; Xu, Y. CO₂ electrochemical reduction at thiolate-modified bulk Au electrodes. *Catal. Sci. Technol.* **2019**, *9* (10), 2689–2701.
- (15) Nitopi, S.; Bertheussen, E.; Scott, S. B.; Liu, X.; Engstfeld, A. K.; Horch, S.; Seger, B.; Stephens, I. E. L.; Chan, K.; Hahn, C.; Norskov, J. K.; Jaramillo, T. F.; Chorkendorff, I. Progress and Perspectives of Electrochemical CO₂ Reduction on Copper in Aqueous Electrolyte. *Chem. Rev.* **2019**, *119* (12), 7610–7672.
- (16) Xie, H.; Wang, T.; Liang, J.; Li, Q.; Sun, S. Cu-based nanocatalysts for electrochemical reduction of CO₂. *Nano Today* **2018**, *21*, 41–54.
- (17) Wang, X.; de Araujo, J. F.; Ju, W.; Bagger, A.; Schmies, H.; Kuhl, S.; Rossmeisl, J.; Strasser, P. Mechanistic reaction pathways of enhanced ethylene yields during electroreduction of CO₂-CO co-feeds on Cu and Cu-tandem electrocatalysts. *Nat. Nanotechnol.* **2019**, *14* (11), 1063–1070.
- (18) Garza, A. J.; Bell, A. T.; Head-Gordon, M. Mechanism of CO₂ Reduction at Copper Surfaces: Pathways to C₂ Products. *ACS Catal.* **2018**, *8* (2), 1490–1499.
- (19) Yuan, X.; Wu, Y.; Jiang, B.; Wu, Z.; Tao, Z.; Lu, X.; Liu, J.; Qian, T.; Lin, H.; Zhang, Q. Interface Engineering of Silver-Based Heterostructures for CO₂ Reduction Reaction. *ACS Appl. Mater. Interfaces* **2020**, *12* (50), 56642–56649.
- (20) Liu, S.; Tao, H.; Zeng, L.; Liu, Q.; Xu, Z.; Liu, Q.; Luo, J. L. Shape-Dependent Electrocatalytic Reduction of CO₂ to CO on Triangular Silver Nanoplates. *J. Am. Chem. Soc.* **2017**, *139* (6), 2160–2163.
- (21) Liu, H.; Liu, J.; Yang, B. Computational insights into the strain effect on the electrocatalytic reduction of CO₂ to CO on Pd surfaces. *Phys. Chem. Chem. Phys.* **2020**, *22* (17), 9600–9606.
- (22) Chang, Q.; Kim, J.; Lee, J. H.; Kattel, S.; Chen, J. G.; Choi, S. I.; Chen, Z. Boosting Activity and Selectivity of CO₂ Electroreduction by Pre-Hydridizing Pd Nanocubes. *Small* **2020**, *16* (49), No. e2005305.
- (23) He, Q.; Lee, J. H.; Liu, D.; Liu, Y.; Lin, Z.; Xie, Z.; Hwang, S.; Kattel, S.; Song, L.; Chen, J. G. Accelerating CO₂ Electroreduction to

- CO Over Pd Single-Atom Catalyst. *Adv. Funct. Mater.* **2020**, *30* (17), No. 2000407.
- (24) Nguyen, D. L. T.; Kim, Y.; Hwang, Y. J.; Won, D. H. Progress in development of electrocatalyst for CO₂ conversion to selective CO production. *Carbon Energy* **2020**, *2*, 72–98.
- (25) Wang, J.; Hu, H.; Lu, S.; Hu, J.; Zhu, H.; Duan, F.; Du, M. Conductive metal and covalent organic frameworks for electrocatalysis: design principles, recent progress and perspective. *Nanoscale* **2022**, *14* (2), 277–288.
- (26) Nafiujiama, M.; Nurunnabi, M., Chapter 5 - Graphene and 2D Materials for Phototherapy. In *Biomedical Applications of Graphene and 2D Nanomaterials*, Nurunnabi, M.; McCarthy, J. R., Eds.; Elsevier, 2019; pp 105–117.
- (27) Tedstone, A. A.; Lewis, D. J.; O'Brien, P. Synthesis, Properties, and Applications of Transition Metal-Doped Layered Transition Metal Dichalcogenides. *Chem. Mater.* **2016**, *28* (7), 1965–1974.
- (28) Peng, Z.; Chen, X.; Fan, Y.; Srolovitz, D. J.; Lei, D. Strain engineering of 2D semiconductors and graphene: from strain fields to band-structure tuning and photonic applications. *Light: Sci. Appl.* **2020**, *9* (1), 190.
- (29) Dong, R.; Kuljanishvili, I. Review Article: Progress in fabrication of transition metal dichalcogenides heterostructure systems. *J. Vac. Sci. Technol. B* **2017**, *35* (3), No. 030803.
- (30) Ahmed, S.; Yi, J. Two-Dimensional Transition Metal Dichalcogenides and Their Charge Carrier Mobilities in Field-Effect Transistors. *Nano-Micro Lett.* **2017**, *9* (4), 50.
- (31) Chhowalla, M.; Shin, H. S.; Eda, G.; Li, L.-J.; Loh, K. P.; Zhang, H. The chemistry of two-dimensional layered transition metal dichalcogenide nanosheets. *Nat. Chem.* **2013**, *5* (4), 263–275.
- (32) Wang, Q. H.; Kalantar-Zadeh, K.; Kis, A.; Coleman, J. N.; Strano, M. S. Electronics and optoelectronics of two-dimensional transition metal dichalcogenides. *Nat. Nanotechnol.* **2012**, *7* (11), 699–712.
- (33) Li, H.; Jia, X.; Zhang, Q.; Wang, X. Metallic Transition-Metal Dichalcogenide Nanocatalysts for Energy Conversion. *Chem.* **2018**, *4* (7), 1510–1537.
- (34) Manzeli, S.; Ovchinnikov, D.; Pasquier, D.; Yazev, O. V.; Kis, A. 2D transition metal dichalcogenides. *Nat. Rev. Mater.* **2017**, *2* (8), 17033.
- (35) Deng, S.; Li, L.; Li, M. Stability of direct band gap under mechanical strains for monolayer MoS₂, MoSe₂, WS₂ and WSe₂. *Phys. E* **2018**, *101*, 44–49.
- (36) Mujib, S. B.; Ren, Z.; Mukherjee, S.; Soares, D. M.; Singh, G. Design, characterization, and application of elemental 2D materials for electrochemical energy storage, sensing, and catalysis. *Mater. Adv.* **2020**, *1* (8), 2562–2591.
- (37) Kang, K.; Chen, S.; Yang, E.-H., 12 - Synthesis of transition metal dichalcogenides. In *Synthesis, Modeling, and Characterization of 2D Materials, and Their Heterostructures*, Yang, E.-H.; Datta, D.; Ding, J.; Hader, G., Eds.; Elsevier, 2020; pp 247–264.
- (38) Yang, H.; Kim, S. W.; Chhowalla, M.; Lee, Y. H. Structural and quantum-state phase transitions in van der Waals layered materials. *Nat. Phys.* **2017**, *13* (10), 931–937.
- (39) Cavin, J.; Ahmadiparidari, A.; Majidi, L.; Thind, A. S.; Misal, S. N.; Prajapati, A.; Hemmat, Z.; Rastegar, S.; Beukelman, A.; Singh, M. R.; Unocic, K. A.; Salehi-Khojin, A.; Mishra, R. 2D High-Entropy Transition Metal Dichalcogenides for Carbon Dioxide Electrocatalysis. *Adv. Mater.* **2021**, *33* (31), No. 2100347.
- (40) Liu, X.; Yang, H.; He, J.; Liu, H.; Song, L.; Li, L.; Luo, J. Highly Active, Durable Ultrathin MoTe₂ Layers for the Electroreduction of CO₂ to CH₄. *Small* **2018**, *14* (16), No. 1704049.
- (41) Li, X.; Wang, S.; Li, L.; Zu, X.; Sun, Y.; Xie, Y. Opportunity of Atomically Thin Two-Dimensional Catalysts for Promoting CO₂ Electroreduction. *Acc. Chem. Res.* **2020**, *53* (12), 2964–2974.
- (42) Pan, J.; Wang, R.; Xu, X.; Hu, J.; Ma, L. Transition metal doping activated basal-plane catalytic activity of two-dimensional 1T'-ReS₂ for hydrogen evolution reaction: a first-principles calculation study. *Nanoscale* **2019**, *11* (21), 10402–10409.
- (43) Chan, K.; Tsai, C.; Hansen, H. A.; Nørskov, J. K. Molybdenum Sulfides and Selenides as Possible Electrocatalysts for CO₂ Reduction. *ChemCatChem.* **2014**, *6* (7), 1899–1905.
- (44) Asadi, M.; Kim, K.; Liu, C.; Addepalli, A. V.; Abbasi, P.; Yasaei, P.; Phillips, P.; Behranginia, A.; Cerrato, J. M.; Haasch, R.; Zapol, P.; Kumar, B.; Klie, R. F.; Abiade, J.; Curtiss, L. A.; Salehi-Khojin, A. Nanostructured transition metal dichalcogenide electrocatalysts for CO₂ reduction in ionic liquid. *Science* **2016**, *353* (6298), 467–470.
- (45) Asadi, M.; Kumar, B.; Behranginia, A.; Rosen, B. A.; Baskin, A.; Repnin, N.; Pisasale, D.; Phillips, P.; Zhu, W.; Haasch, R.; Klie, R. F.; Král, P.; Abiade, J.; Salehi-Khojin, A. Robust carbon dioxide reduction on molybdenum disulphide edges. *Nat. Commun.* **2014**, *5* (1), 4470.
- (46) Abbasi, P.; Asadi, M.; Liu, C.; Sharifi-Asl, S.; Sayahpour, B.; Behranginia, A.; Zapol, P.; Shahbazian-Yassar, R.; Curtiss, L. A.; Salehi-Khojin, A. Tailoring the Edge Structure of Molybdenum Disulfide toward Electrocatalytic Reduction of Carbon Dioxide. *ACS Nano* **2017**, *11* (1), 453–460.
- (47) Li, H.; Liu, X.; Chen, S.; Yang, D.; Zhang, Q.; Song, L.; Xiao, H.; Zhang, Q.; Gu, L.; Wang, X. Edge-Exposed Molybdenum Disulfide with N-Doped Carbon Hybridization: A Hierarchical Hollow Electrocatalyst for Carbon Dioxide Reduction. *Adv. Energy Mater.* **2019**, *9* (18), No. 1900072.
- (48) Wu, X.; Zhang, H.; Zhang, J.; Lou, X. W. D. Recent Advances on Transition Metal Dichalcogenides for Electrochemical Energy Conversion. *Adv. Mater.* **2021**, *33* (38), No. e2008376.
- (49) Lihter, M.; Graf, M.; Iveković, D.; Zhang, M.; Shen, T.-H.; Zhao, Y.; Macha, M.; Tileli, V.; Radenovic, A. Electrochemical Functionalization of Selectively Addressed MoS₂ Nanoribbons for Sensor Device Fabrication. *ACS Appl. Nano Mater.* **2021**, *4* (2), 1076–1084.
- (50) Han, J. H.; Kim, H. K.; Baek, B.; Han, J.; Ahn, H. S.; Baik, M. H.; Cheon, J. Activation of the Basal Plane in Two Dimensional Transition Metal Chalcogenide Nanostructures. *J. Am. Chem. Soc.* **2018**, *140* (42), 13663–13671.
- (51) Cai, Z.; Liu, B.; Zou, X.; Cheng, H.-M. Chemical Vapor Deposition Growth and Applications of Two-Dimensional Materials and Their Heterostructures. *Chem. Rev.* **2018**, *118* (13), 6091–6133.
- (52) Zhou, M.; Wang, W.; Lu, J.; Ni, Z. How defects influence the photoluminescence of TMDCs. *Nano Res.* **2021**, *14* (1), 29–39.
- (53) Zhao, S.; Liu, A.; Li, Y.; Wen, Y.; Gao, X.; Chen, Q. Boosting the Electrocatalytic CO₂ Reduction Reaction by Nanostructured Metal Materials via Defects Engineering. *Nanomaterials* **2022**, *12* (14), 2389.
- (54) Singh, S.; Modak, A.; Pant, K. K.; Sinhamahapatra, A.; Biswas, P. MoS₂-Nanosheets-Based Catalysts for Photocatalytic CO₂ Reduction: A Review. *ACS Appl. Nano Mater.* **2021**, *4* (9), 8644–8667.
- (55) Meier, A. J.; Garg, A.; Sutter, B.; Kuhn, J. N.; Bhethanabotla, V. R. MoS₂ Nanoflowers as a Gateway for Solar-Driven CO₂ Photoreduction. *ACS Sustainable Chem. Eng.* **2019**, *7* (1), 265–275.
- (56) Nguyen, A. D.; Nguyen, T. K.; Le, C. T.; Kim, S.; Ullah, F.; Lee, Y.; Lee, S.; Kim, K.; Lee, D.; Park, S.; Bae, J.-S.; Jang, J. I.; Kim, Y. S. Nitrogen-Plasma-Treated Continuous Monolayer MoS₂ for Improving Hydrogen Evolution Reaction. *ACS Omega* **2019**, *4* (25), 21509–21515.
- (57) Huang, Y.-F.; Liao, K.-W.; Fahmi, F. R. Z.; Modak, V. A.; Tsai, S.-H.; Ke, S.-W.; Wang, C.-H.; Chen, L.-C.; Chen, K.-H. Thickness-Dependent Photocatalysis of Ultra-Thin MoS₂ Film for Visible-Light-Driven CO₂ Reduction. *Catalysts* **2021**, *11* (11), 1295.
- (58) Ji, Y.; Nørskov, J.; Chan, K. Scaling Relations on Basal Plane Vacancies of Transition Metal Dichalcogenides for CO₂ Reduction. *J. Phys. Chem. C* **2019**, *123*, No. 8b11628.
- (59) Li, W.; Liu, G.; Li, J.; Wang, Y.; Ricardez-Sandoval, L.; Zhang, Y.; Zhang, Z. Hydrogen evolution reaction mechanism on 2H-MoS₂ electrocatalyst. *Appl. Surf. Sci.* **2019**, *498*, No. 143869.
- (60) Mehta, A. N.; Mo, J.; Pourtois, G.; Dabral, A.; Groven, B.; Bender, H.; Favia, P.; Caymax, M.; Vandervorst, W. Grain-Boundary-Induced Strain and Distortion in Epitaxial Bilayer MoS₂ Lattice. *J. Phys. Chem. C* **2020**, *124* (11), 6472–6478.

- (61) Huang, H.; Jung, H.; Jun, H.; Woo, D.; Han, J. W.; Lee, J. Design of grain boundary enriched bimetallic borides for enhanced hydrogen evolution reaction. *Chem. Eng. J.* **2021**, *405*, No. 126977.
- (62) He, Y.; Tang, P.; Hu, Z.; He, Q.; Zhu, C.; Wang, L.; Zeng, Q.; Golani, P.; Gao, G.; Fu, W.; Huang, Z.; Gao, C.; Xia, J.; Wang, X.; Wang, X.; Zhu, C.; Ramasse, Q. M.; Zhang, A.; An, B.; Zhang, Y.; Martí-Sánchez, S.; Morante, J. R.; Wang, L.; Tay, B. K.; Yakobson, B. I.; Trampert, A.; Zhang, H.; Wu, M.; Wang, Q. J.; Arbiol, J.; Liu, Z. Engineering grain boundaries at the 2D limit for the hydrogen evolution reaction. *Nat. Commun.* **2020**, *11* (1), 57.
- (63) Dong, S.; Wang, Z. Grain Boundaries Trigger Basal Plane Catalytic Activity for the Hydrogen Evolution Reaction in Monolayer MoS₂. *Electrocatalysis* **2018**, *9* (6), 744–751.
- (64) Mondal, S.; De, S. K.; Jana, R.; Roy, A.; Mukherjee, M.; Datta, A.; Satpati, B.; Senapati, D. Unveiling the Excellent Electrocatalytic Activity of Grain-Boundary Enriched Anisotropic Pure Gold Nanostructures toward Hydrogen Evolution Reaction: A Combined Approach of Experiment and Theory. *ACS Appl. Energy Mater.* **2021**, *4* (4), 3017–3032.
- (65) Ouyang, Y.; Ling, C.; Chen, Q.; Wang, Z.; Shi, L.; Wang, J. Activating Inert Basal Planes of MoS₂ for Hydrogen Evolution Reaction through the Formation of Different Intrinsic Defects. *Chem. Mater.* **2016**, *28* (12), 4390–4396.
- (66) Feng, X.; Jiang, K.; Fan, S.; Kanan, M. W. A Direct Grain-Boundary-Activity Correlation for CO Electroreduction on Cu Nanoparticles. *ACS Cent. Sci.* **2016**, *2* (3), 169–174.
- (67) Dong, C.; Fu, J.; Liu, H.; Ling, T.; Yang, J.; Qiao, S. Z.; Du, X.-W. Tuning the selectivity and activity of Au catalysts for carbon dioxide electroreduction via grain boundary engineering: a DFT study. *J. Mater. Chem. A* **2017**, *5* (15), 7184–7190.
- (68) Feng, X.; Jiang, K.; Fan, S.; Kanan, M. W. Grain-Boundary-Dependent CO₂ Electroreduction Activity. *J. Am. Chem. Soc.* **2015**, *137* (14), 4606–4609.
- (69) Zhu, E.; Xue, W.; Wang, S.; Yan, X.; Zhou, J.; Liu, Y.; Cai, J.; Liu, E.; Jia, Q.; Duan, X.; Li, Y.; Heinz, H.; Huang, Y. Enhancement of oxygen reduction reaction activity by grain boundaries in platinum nanostructures. *Nano Res.* **2020**, *13* (12), 3310–3314.
- (70) Zhang, R.; Wang, L.; Ma, Y.-H.; Pan, L.; Gao, R.; Li, K.; Zhang, X.; Zou, J.-J. Grain boundaries modified uniformly-conjoint metal/oxides via binder strategy as efficient bifunctional electrocatalysts. *J. Mater. Chem. A* **2019**, *7* (16), 10010–10018.
- (71) Wang, L.; Qin, T.; Wang, J.; Wang, J.; Zhang, J.; Cong, Y.; Li, X.-K.; Li, Y. Grain boundary engineering of Co ₃O ₄ nanomeshes for efficient electrochemical oxygen evolution. *Nanotechnology* **2020**, *31* (45), 455401.
- (72) Wang, J.-Q.; Xi, C.; Wang, M.; Shang, L.; Mao, J.; Dong, C.-K.; Liu, H.; Kulinich, S. A.; Du, X.-W. Laser-Generated Grain Boundaries in Ruthenium Nanoparticles for Boosting Oxygen Evolution Reaction. *ACS Catal.* **2020**, *10* (21), 12575–12581.
- (73) Liu, X.-J.; Yin, X.; Sun, Y.-D.; Yu, F.-J.; Gao, X.-W.; Fu, L.-J.; Wu, Y.-P.; Chen, Y.-H. Interlaced Pd–Ag nanowires rich in grain boundary defects for boosting oxygen reduction electrocatalysis. *Nanoscale* **2020**, *12* (9), 5368–5373.
- (74) Hu, Q.; Qin, Y.; Wang, X.; Zheng, H.; Gao, K.; Yang, H.; Zhang, P.; Shao, M.; He, C. Grain Boundaries Engineering of Hollow Copper Nanoparticles Enables Highly Efficient Ammonia Electrosynthesis from Nitrate. *CCS Chem.* **2021**, *4* (6), 2053–2064.
- (75) Qin, Y.; Wu, D.-Y.; Su, Y. The Effect of Grain Boundary in Hexagonal Boron Nitride on Catalytic Activity of Nitrogen Reduction Reaction. *Appl. Surf. Sci.* **2022**, *593*, No. 153468, DOI: 10.1016/j.apusc.2022.153468.
- (76) Upmanyu, M.; Srolovitz, D. J.; Shvinderman, L. S.; Gottstein, G. Vacancy Generation During Grain Boundary Migration. *Interface Sci.* **1998**, *6*, 289–300.
- (77) Millett, P. C.; Aidhy, D. S.; Desai, T.; Phillpot, S. R.; Wolf, D. Grain-boundary source/sink behavior for point defects: An atomistic simulation study. *Int. J. Mater. Res.* **2009**, *100* (4), 550–555.
- (78) Gleiter, H. Grain boundaries as point defect sources or sinks—Diffusional creep. *Acta Metall.* **1979**, *27* (2), 187–192.
- (79) Gao, N.; Guo, Y.; Zhou, S.; Bai, Y.; Zhao, J. Structures and Magnetic Properties of MoS₂ Grain Boundaries with Antisite Defects. *J. Phys. Chem. C* **2017**, *121* (22), 12261–12269.
- (80) Varrla, E.; Backes, C.; Paton, K. R.; Harvey, A.; Gholamvand, Z.; McCauley, J.; Coleman, J. N. Large-Scale Production of Size-Controlled MoS₂ Nanosheets by Shear Exfoliation. *Chem. Mater.* **2015**, *27* (3), 1129–1139.
- (81) Chen, Y.-X.; Wu, C.-W.; Kuo, T.-Y.; Chang, Y.-L.; Jen, M.-H.; Chen, I. W. P. Large-Scale Production of Large-Size Atomically Thin Semiconducting Molybdenum Dichalcogenide Sheets in Water and Its Application for Supercapacitor. *Sci. Rep.* **2016**, *6* (1), 26660.
- (82) Nguyen, V. T.; Ha, S.; Yeom, D.-I.; Ahn, Y. H.; Lee, S.; Park, J.-Y. Large-scale chemical vapor deposition growth of highly crystalline MoS₂ thin films on various substrates and their optoelectronic properties. *Curr. Appl. Phys.* **2019**, *19* (10), 1127–1131.
- (83) Wang, Z.; Liu, X.; Zhu, J.; You, S.; Bian, K.; Zhang, G.; Feng, J.; Jiang, Y. Local engineering of topological phase in monolayer MoS₂. *Sci. Bull.* **2019**, *64* (23), 1750–1756.
- (84) Ataca, C.; Topsakal, M.; Aktürk, E.; Ciraci, S. A Comparative Study of Lattice Dynamics of Three- and Two-Dimensional MoS₂. *J. Phys. Chem. C* **2011**, *115* (33), 16354–16361.
- (85) Fu, Y.-D.; Feng, X.-X.; Yan, M.-F.; Wang, K.; Wang, S.-Y. First principle study on electronic structure and optical phonon properties of 2H-MoS₂. *Phys. B* **2013**, *426*, 103–107.
- (86) Yu, Z. G.; Zhang, Y.-W.; Yakobson, B. I. An Anomalous Formation Pathway for Dislocation-Sulfur Vacancy Complexes in Polycrystalline Monolayer MoS₂. *Nano Lett.* **2015**, *15* (10), 6855–6861.
- (87) Li, H.; Tsai, C.; Koh, A. L.; Cai, L.; Contryman, A. W.; Frapapane, A. H.; Zhao, J.; Han, H. S.; Manoharan, H. C.; Abild-Pedersen, F.; Nørskov, J. K.; Zheng, X. Activating and optimizing MoS₂ basal planes for hydrogen evolution through the formation of strained sulphur vacancies. *Nat. Mater.* **2016**, *15* (1), 48–53.
- (88) Mao, X.; Wang, L.; Xu, Y.; Li, Y. Modulating the MoS₂ Edge Structures by Doping Transition Metals for Electrocatalytic CO₂ Reduction. *J. Phys. Chem. C* **2020**, *124* (19), 10523–10529.
- (89) Marcandalli, G.; Goyal, A.; Koper, M. T. M. Electrolyte Effects on the Faradaic Efficiency of CO₂ Reduction to CO on a Gold Electrode. *ACS Catal.* **2021**, *11* (9), 4936–4945.
- (90) Gao, F.-Y.; Bao, R.-C.; Gao, M.-R.; Yu, S.-H. Electrochemical CO₂-to-CO conversion: electrocatalysts, electrolytes, and electrolyzers. *J. Mater. Chem. A* **2020**, *8* (31), 15458–15478.
- (91) Zheng, T.; Jiang, K.; Wang, H. Recent Advances in Electrochemical CO₂-to-CO Conversion on Heterogeneous Catalysts. *Adv. Mater.* **2018**, *30* (48), No. 1802066.
- (92) Hansen, H. A.; Varley, J. B.; Peterson, A. A.; Nørskov, J. K. Understanding Trends in the Electrocatalytic Activity of Metals and Enzymes for CO₂ Reduction to CO. *J. Phys. Chem. Lett.* **2013**, *4* (3), 388–392.
- (93) Kortlever, R.; Shen, J.; Schouten, K. J. P.; Calle-Vallejo, F.; Koper, M. T. M. Catalysts and Reaction Pathways for the Electrochemical Reduction of Carbon Dioxide. *J. Phys. Chem. Lett.* **2015**, *6* (20), 4073–4082.
- (94) Nørskov, J. K.; Rossmeisl, J.; Logadottir, A.; Lindqvist, L.; Kitchin, J. R.; Bligaard, T.; Jónsson, H. Origin of the Overpotential for Oxygen Reduction at a Fuel-Cell Cathode. *J. Phys. Chem. B* **2004**, *108* (46), 17886–17892.
- (95) Kresse, G.; Hafner, J. Ab initio molecular dynamics for liquid metals. *Phys. Rev. B* **1993**, *47* (1), 558–561.
- (96) Kresse, G.; Furthmüller, J. Efficiency of ab-initio total energy calculations for metals and semiconductors using a plane-wave basis set. *Comput. Mater. Sci.* **1996**, *6* (1), 15–50.
- (97) Kresse, G.; Furthmüller, J. Efficient iterative schemes for ab initio total-energy calculations using a plane-wave basis set. *Phys. Rev. B* **1996**, *54* (16), 11169–11186.
- (98) Kresse, G.; Joubert, D. From ultrasoft pseudopotentials to the projector augmented-wave method. *Phys. Rev. B* **1999**, *59* (3), 1758–1775.

- (99) Kresse, G.; Hafner, J. Norm-conserving and ultrasoft pseudopotentials for first-row and transition elements. *J. Phys.: Condens. Matter* **1994**, *6* (40), 8245–8257.
- (100) Blöchl, P. E. Projector augmented-wave method. *Phys. Rev. B* **1994**, *50* (24), 17953–17979.
- (101) Grimme, S. Semiempirical GGA-type density functional constructed with a long-range dispersion correction. *J. Comput. Chem.* **2006**, *27* (15), 1787–1799.
- (102) Sabatier, P. *La catalyse en chimie organique*, 1920.
- (103) Xie, Y.; Li, X.; Wang, Y.; Li, B.; Yang, L.; Zhao, N.; Liu, M.; Wang, X.; Yu, Y.; Liu, J. M. Reaction mechanisms for reduction of CO₂ to CO on monolayer MoS₂. *Appl. Surf. Sci.* **2020**, *499*, No. 143964.
- (104) Chu, S.; Ou, P.; Ghamari, P.; Vanka, S.; Zhou, B.; Shih, I.; Song, J.; Mi, Z. Photoelectrochemical CO₂ Reduction into Syngas with the Metal/Oxide Interface. *J. Am. Chem. Soc.* **2018**, *140* (25), 7869–7877.
- (105) Bi, W.; Li, X.; You, R.; Chen, M.; Yuan, R.; Huang, W.; Wu, X.; Chu, W.; Wu, C.; Xie, Y. Surface Immobilization of Transition Metal Ions on Nitrogen-Doped Graphene Realizing High-Efficient and Selective CO₂ Reduction. *Adv. Mater.* **2018**, *30* (18), No. 1706617.
- (106) Kim, D.; Xie, C.; Becknell, N.; Yu, Y.; Karamad, M.; Chan, K.; Crumlin, E. J.; Nørskov, J. K.; Yang, P. Electrochemical Activation of CO₂ through Atomic Ordering Transformations of AuCu Nanoparticles. *J. Am. Chem. Soc.* **2017**, *139* (24), 8329–8336.
- (107) Ouyang, Y.; Shi, L.; Bai, X.; Li, Q.; Wang, J. Breaking scaling relations for efficient CO₂ electrochemical reduction through dual-atom catalysts. *Chem. Sci.* **2020**, *11* (7), 1807–1813.
- (108) Calle-Vallejo, F.; Loffreda, D.; Koper, M. T. M.; Sautet, P. Introducing structural sensitivity into adsorption–energy scaling relations by means of coordination numbers. *Nat. Chem.* **2015**, *7* (5), 403–410.
- (109) Zhu, W.; Zhang, Y.-J.; Zhang, H.; Lv, H.; Li, Q.; Michalsky, R.; Peterson, A. A.; Sun, S. Active and Selective Conversion of CO₂ to CO on Ultrathin Au Nanowires. *J. Am. Chem. Soc.* **2014**, *136* (46), 16132–16135.
- (110) Lim, H.-K.; Shin, H.; Goddard, W. A., III; Hwang, Y. J.; Min, B. K.; Kim, H. Embedding Covalency into Metal Catalysts for Efficient Electrochemical Conversion of CO₂. *J. Am. Chem. Soc.* **2014**, *136* (32), 11355–11361.
- (111) Li, Y.; Su, H.; Chan, S. H.; Sun, Q. CO₂ Electroreduction Performance of Transition Metal Dimers Supported on Graphene: A Theoretical Study. *ACS Catal.* **2015**, *5* (11), 6658–6664.
- (112) Li, J. Oxygen Evolution Reaction in Energy Conversion and Storage: Design Strategies Under and Beyond the Energy Scaling Relationship. *Nano-Micro Lett.* **2022**, *14* (1), 112.
- (113) Lai, Y.; Watkins, N. B.; Rosas-Hernández, A.; Thevenon, A.; Heim, G. P.; Zhou, L.; Wu, Y.; Peters, J. C.; Gregoire, J. M.; Agapie, T. Breaking Scaling Relationships in CO₂ Reduction on Copper Alloys with Organic Additives. *ACS Cent. Sci.* **2021**, *7* (10), 1756–1762.
- (114) Jansonius, R. P.; Reid, L. M.; Virca, C. N.; Berlinguet, C. P. Strain Engineering Electrocatalysts for Selective CO₂ Reduction. *ACS Energy Lett.* **2019**, *4* (4), 980–986.
- (115) Li, Y.; Sun, Q. Recent Advances in Breaking Scaling Relations for Effective Electrochemical Conversion of CO₂. *Adv. Energy Mater.* **2016**, *6* (17), No. 1600463.
- (116) Gor, G. Y.; Huber, P.; Bernstein, N. Adsorption-induced deformation of nanoporous materials—A review. *Applied Physics Reviews* **2017**, *4* (1), No. 011303.
- (117) Wu, X.; Yang, J.; Hou, J. G.; Zhu, Q. Deformation-induced site selectivity for hydrogen adsorption on boron nitride nanotubes. *Phys. Rev. B* **2004**, *69* (15), No. 153411.
- (118) Ding, M.; He, Q.; Wang, G.; Cheng, H.-C.; Huang, Y.; Duan, X. An on-chip electrical transport spectroscopy approach for in situ monitoring electrochemical interfaces. *Nat. Commun.* **2015**, *6* (1), 7867.
- (119) Mayrhofer, K. J. J.; Blizanac, B. B.; Arenz, M.; Stamenkovic, V. R.; Ross, P. N.; Markovic, N. M. The Impact of Geometric and Surface Electronic Properties of Pt-Catalysts on the Particle Size Effect in Electrocatalysis. *J. Phys. Chem. B* **2005**, *109* (30), 14433–14440.
- (120) Huang, B.; Xiao, L.; Lu, J.; Zhuang, L. Spatially Resolved Quantification of the Surface Reactivity of Solid Catalysts. *Angew. Chem., Int. Ed.* **2016**, *55*, 6239–6243.
- (121) Nian, Y.; Wang, Y.; Biswas, A. N.; Chen, X.; Han, Y.; Chen, J. G. Trends and descriptors for tuning CO₂ electroreduction to synthesis gas over Ag and Au supported on transition metal carbides and nitrides. *Chem. Eng. J.* **2021**, *426*, No. 130781.
- (122) Tang, W.; Sanville, E.; Henkelman, G. A grid-based Bader analysis algorithm without lattice bias. *J. Phys.: Condens. Matter* **2009**, *21* (8), No. 084204.
- (123) Zhao, Z.; Chen, Z.; Zhang, X.; Lu, G. Generalized Surface Coordination Number as an Activity Descriptor for CO₂ Reduction on Cu Surfaces. *J. Phys. Chem. C* **2016**, *120* (49), 28125–28130.
- (124) Wang, Y.; Liu, Y.; Liu, W.; Wu, J.; Li, Q.; Feng, Q.; Chen, Z.; Xiong, X.; Wang, D.; Lei, Y. Regulating the coordination structure of metal single atoms for efficient electrocatalytic CO₂ reduction. *Energy Environ. Sci.* **2020**, *13* (12), 4609–4624.